

Confidence interval constraint based regularization framework for PET quantization

F. Kucharczak, F. Ben Bouallegue, O. Strauss, D. Mariano-Goulart

Abstract—In this paper, a new generic regularized reconstruction framework based on confidence interval constraints for tomographic reconstruction is presented. As opposed to usual state-of-the-art regularization methods that try to minimize a cost function expressed as the sum of a data-fitting term and a regularization term weighted by a scalar parameter, the proposed algorithm is a two-step process. The first step concentrates on finding a set of images that relies on direct estimation of confidence intervals for each reconstructed value. Then, the second step uses confidence intervals as a constraint to choose the most appropriate candidate according to a regularization criterion. Two different constraints are proposed in this paper. The first one has the main advantage of strictly ensuring that the regularized solution will respect the interval-valued data-fitting constraint, thus preventing over-smoothing of the solution while offering interesting properties in terms of spatial and statistical bias/variance trade-off. Another regularization proposition based on the design of a smoother constraint also with appealing properties is proposed as an alternative. The competitiveness of the proposed framework is illustrated in comparison to other regularization schemes using analytical and GATE-based simulation and real PET acquisition.

Index Terms—Image reconstruction, positron emission tomography, confidence intervals, constrained regularization, total variation.

I. INTRODUCTION

IN recent decades, Positron Emission Tomography (PET) has gained great interest in many medical fields [1] due to its ability to provide semi-quantitative measures of the radiotracer uptake in a volume of interest. However, PET reconstruction is an ill-posed problem and thus, the most widespread iterative reconstruction algorithms (SIRT-based [2], [3] and ML-EM-based [4], [5]) produce images with undesirable noise amplification and instability under data perturbations that increase with the number of iterations. As a consequence, such algorithms have to be regularized, i.e. the solution of the inverse problem has to be constrained to comply with some prior knowledge. Such regularization is usually performed either by early stopping [6], [7] or by post-processing procedures [8], [9] like filtering or deconvolution. Bayesian

reconstruction procedures like those based on maximum a-posteriori (MAP) [10]–[12] or penalized maximum-likelihood (PML) [13], [14] include a regularization term that fosters spatial smoothness in the estimated PET images.

In recent years, the prevalent use of \mathcal{L}_2 norm based regularization has been questioned in image processing, leading to increasing interest in optimization-based reconstruction techniques using compress sensing approaches [15]. The objective of these approaches is to recover sparse images by solving linear optimization problems involving the \mathcal{L}_1 norm. These approaches were proven to be efficient in problems such as denoising [16], [17], image compression [18], image restoration [19], [20] and inverse problems like super-resolution [21]–[23] and in CT [24], [25]. Since the radiotracer activity distribution in PET may in a first approximation be considered as a piecewise constant function, reconstructing sparse gradient-magnitude images seems completely relevant. This strategy has been proposed to reconstruct sparse gradient-magnitude images in PET [26], [27]. Recent work focusing on edge-preserving regularization via smooth non-quadratic penalties have also been presented using patch-based PML approaches [14] or trust optimization transfer algorithms [28]. A common problem currently faced by most of these approaches is that a regularization hyper-parameter is needed to balance data fidelity and regularization criterion. It makes the trade-off between the two conflicting objectives dependent on the hyper-parameter involved in this combination [29].

We propose an innovative approach based on a two-step process to solve this trade-off problem. First, we define a convex set \mathbf{D} of images complying with the data fidelity criterion and then we seek in \mathbf{D} for the image that best fulfills a chosen regularization criterion. Such an approach has recently been proposed to achieve super-resolution reconstruction [29], JPEG deblocking [30], [31], CT reconstruction [24] and Total Variation (TV) optimization-based reconstruction in PET [32]. However, within this approach, one of the main challenges concerns the definition of a meaningful convex set \mathbf{D} to be used as a data fidelity constraint for regularization. Recent works has been carried out in the open field of statistical variability estimation of PET reconstructed data. In [33], [34], authors proposed extensions of both SIRT and ML-EM algorithms that reconstruct voxel-wise stable confidence intervals (CI) instead of scalar values. Here, we propose \mathbf{D} to be these meaningful, reliable and stable CI. The generic reconstruction we propose consists in selecting the image that best minimizes a chosen regularization criterion under the constraint of \mathbf{D} . In this paper, the choice was made to use the widely known TV regularization criteria.

F. Kucharczak was with Siemens Healthineers, Saint-Denis, France, LIRMM, Univ. Montpellier, France, and Department of Nuclear Medicine, Montpellier University Hospital, 34295 Montpellier cedex 5, France. F. Ben Bouallegue and D. Mariano-Goulart were with Department of Nuclear Medicine, Montpellier University Hospital, 34295 Montpellier cedex 5, France and PhyMedExp, Univ. Montpellier, INSERM U1046, CNRS UMR 9214, 34295 Montpellier cedex 5, France. O. Strauss was with LIRMM, Univ. Montpellier, France.

Copyright (c) 2018 IEEE. Personal use of this material is permitted. However, permission to use this material for any other purposes must be obtained from the IEEE by sending a request to pubs-permissions@ieee.org.

In this paper, we first briefly recall the fundamentals of CI reconstruction in PET in Section II-A, then present the TV constrained regularized step in II-B. In Section II-C, the full methodology of the reconstruction procedure is summarized. Finally, Section III presents the competitiveness of the presented algorithm in terms of the bias/variance trade-off in both spatial and statistical terms using analytic and GATE [35] simulation and real PET acquisition of phantom and clinical data. Finally, the conclusions and perspectives are discussed in Section IV.

II. THE CONSTRAINED, REGULARIZED RECONSTRUCTION FRAMEWORK

In this paper, we propose a new reconstruction framework based on CI constrained TV regularization. The novelty of this approach resides in the fact that the regularized reconstruction technique deals with inverse problem resolution in two steps. Instead of trying to balance a data-fitting term and a regularization term in the same reconstruction process, we instead propose to first focus on reconstructing a convex set of admissible solutions that ensure the data fidelity and then, in a second step, to select the most appropriate image according to a regularization criterion under the constraint established in step one.

A. First step - data-fitting constraint reconstruction

In PET, the problem of assessing the uncertainty associated with the reconstructed activity distribution has been addressed using numerous approaches. However, none of them explicitly presented algorithms for direct estimation of CI until [34]. The NIBEM (rsp. NIBART) algorithm, presented in [34] (rsp. [33]) is an extension of the widely known ML-EM (rsp. SIRT) algorithm. Its distinctive characteristic is, for each pixel, to reconstruct intervals with appealing properties instead of scalar values. This section presents a brief overview of the founding principles of this algorithm.

1) *Discrete-to-continuous interplay*: Reconstructing a tomographic image involves inverting a model that describes the projection of the studied distribution onto a finite set of projection bins.

As this projection model is assumed to be linear, it can be computed using a system matrix R , also called a Radon matrix, whose $(i, j)^{th}$ element stands for the probability of a photon emitted in the i^{th} pixel to reach the j^{th} detector. Considering this model, the projection operator \mathcal{P} and its dual operator, the back-projection operator \mathcal{B} , can be defined by:

$$\mathcal{P}(f)_j = \sum_{i=1}^N R_{i,j} f_i, \quad (1)$$

$$\mathcal{B}(p)_i = \sum_{j=1}^M R_{i,j} p_j, \quad (2)$$

with $f \in \mathbb{R}^N$ being the image to reconstruct and $p \in \mathbb{R}^M$ the measurement vector.

Although the projection model usually requires the activity distribution to be continuous, the activity image f is

reconstructed on a discrete grid whose sampling is arbitrarily set according to the resolution of the PET device. Thus, the reconstruction makes intensive use of kernel-based interpolation to ensure this discrete-to-continuous interplay. Modeling the interplay between the discrete reconstruction space and the underlying continuous space, where the problem can be formulated, impacts the resulting projected values. In [36], the authors propose to reduce the impact of arbitrarily choosing a kernel by switching to a method that computes all projections that could have been obtained by using all possible interpolation kernels having a bounded support. By construction, all of these kernels form a continuous convex set (i.e. if two kernels belong to the set, any linear combination of those belongs to the set). Let \mathcal{K} be this set, then the interval-valued projection operator they propose can be expressed as: $[p_j] = [\min_{\kappa \in \mathcal{K}} (\mathcal{P}_\kappa(f)_j); \max_{\kappa \in \mathcal{K}} (\mathcal{P}_\kappa(f)_j)]$, with \mathcal{P}_κ being the projection operator based on the interpolation kernel κ . The appealing property of this framework is that, since the spread of the resulting intervals reflects the range of possible projections, it is thus linked to local variations in the projections. As pointed out in [37], poor consensus on the projected values, i.e. a wide interval spread, is a marker of the effect of noise on the projections. Using the concave capacities theory [38], it is possible to build an interval-valued projection operator $\overline{\mathcal{P}}$ that pools all projectors that would have been obtained by using all possible four-neighbor based interpolations that could ensure the discrete-to-continuous interplay. The theoretical justifications for $\overline{\mathcal{P}}$ are presented in [36]. Practical details about the implementation of $\overline{\mathcal{P}}$ and information on how it can be used for tomographic reconstruction can be found in [34], where a graphical illustration (Fig. 4 of [34]) and the corresponding pseudo-code (Procedure 1 of [34]) to compute the upper projection of a four-pixel image is presented. With this example, computation of the lower bound is straightforward. Using the so-defined interval-valued projector $\overline{\mathcal{P}}$, it has been shown in [33], [34] that SIRT and ML-EM algorithms can be extended to produce interval-valued reconstructions.

2) *Interval arithmetic*: As the SIRT and ML-EM reconstruction algorithms require vector element-wise arithmetical operations and since the operator \mathcal{P} is replaced by its imprecise extension $\overline{\mathcal{P}}$, the SIRT and ML-EM interval-based extensions require interval-valued arithmetical operations to be performed. Let us consider $[a] = [\underline{a}, \overline{a}]$ a real-valued interval whose lower bound is \underline{a} and upper bound is \overline{a} . Using real intervals, Minkowski \odot and dual Minkowski \boxminus arithmetical operators are necessary (with $\cdot \in \{+, -, \times, / \}$). They are defined, with $[a]$ and $[b]$ being two real intervals, as:

$$[a] \odot [b] = [\underline{a} - \overline{b}, \overline{a} - \underline{b}], \quad (3)$$

$$[a] \boxplus [b] = [\underline{a} + \overline{b}, \overline{a} + \underline{b}], \quad (4)$$

and with $[a]$ and $[b]$ being two real positive intervals, as:

$$[a] \oslash [b] = [\underline{a}/\overline{b}, \overline{a}/\underline{b}], \quad (5)$$

$$[a] \boxtimes [b] = [\underline{a} \times \overline{b}, \overline{a} \times \underline{b}], \quad (6)$$

Note also that for any $\lambda \in \mathbf{R}^+$, $\lambda \times [a] = [\lambda \times \underline{a}, \lambda \times \bar{a}]$. The interval-based arithmetical formalism is not in the scope of this paper but more details can be found in [33], [34].

3) *CI reconstruction*: NIBART [33] and NIBEM [34] algorithms can be seen as straightforward interval-based extensions of ML-EM and ART algorithms. As their precise version, these algorithms are iterative. With k being the current iteration and $[\mathbf{f}^k]$ the reconstructed interval-based image at iteration k , both NIBART and NIBEM iterative schemes are defined as:

$$\text{NIBART: } [\mathbf{f}^{k+1}] = \lambda \mathcal{B}^* ([p] \ominus \overline{\mathcal{P}}([\mathbf{f}^k])) \boxplus [\mathbf{f}^k], \quad (7)$$

$$\text{NIBEM: } [\mathbf{f}^{k+1}] = \mathcal{B}^* ([p] \oslash \overline{\mathcal{P}}([\mathbf{f}^k])) \boxtimes [\mathbf{f}^k], \quad (8)$$

with $[p] = [p, p]$ being the measurement vector, $\lambda \in [0, 1]$ a relaxation parameter and \mathcal{B}^* the normalized version of the back-projection operator defined in Eq. (2). In first step of Fig. 1, NIBEM reconstruction is schematically decomposed to facilitate the understanding of Eq. (8).

In [34], it has been highlighted that the reconstructed intervals $[\mathbf{f}]$ reflect statistical variability of the reconstructed values and can be considered as reliable CI, with the confidence value of these intervals being around 90%. It has also been shown in [34] that the estimated CI can be considered as stable and independent of the reconstructed value and the noise level. We propose here to consider the convex set $[\mathbf{f}]$ as a data-fitting constraint to perform TV regularization and prevent over-smoothing of the solution.

B. Second step - regularized selection

The data fidelity constraint used in the proposed framework is the interval-valued image $[\mathbf{f}]$ reconstructed in the first step of Section II-A. $[\mathbf{f}]$ represents the convex-set of admissible images within which the function that best fits a regularization criterion ϵ_2 is constrained. With \mathbf{f} denoting the regularized image, the constrained optimization problem to solve can be formulated as the follows:

$$\min_{\mathbf{f} \in \mathbb{R}^N} \epsilon_2(\mathbf{f}) + g_{[\mathbf{f}]}(\mathbf{f}). \quad (9)$$

with ϵ_2 being a convex regularization criterion and g being the data fitting constraint relative to the interval-valued image $[\mathbf{f}]$ reconstructed in the first step. For computability purposes, ϵ_2 and g are assumed to be proper, convex and lower-semi-continuous (l.s.c) functions.

The convex optimization problem expressed in Eq. (9) involving a sum of two convex functions is common, and numerous convex optimization algorithms have been presented in the literature [39]. Here, we use the primal-dual Chambolle Pock algorithm [40] that was already used for CT convex optimization-based reconstruction [25].

The proximal formulation of the primal-dual Chambolle-Pock algorithm can be written, to solve Eq. (9), as:

$$\begin{cases} v^{(k+1)} = \text{prox}_{\nu \epsilon_2^*}(v^{(k)} + \nu w^{(k)}) \\ \mathbf{f}^{(k+1)} = \text{prox}_{\mu g}(\mathbf{f}^{(k)} - \mu v^{(k+1)}) \\ w^{(k+1)} = \mathbf{f}^{(k+1)} + \theta(\mathbf{f}^{(k+1)} - \mathbf{f}^{(k)}), \end{cases} \quad (10)$$

with $\text{prox}_F(\mathbf{X}) = \underset{\mathbf{Y}}{\text{argmin}} (F(\mathbf{Y}) + \frac{1}{2} \|\mathbf{X} - \mathbf{Y}\|_2^2)$, $\|\cdot\|_2$ being the \mathcal{L}_2 norm, μ , ν and θ being real numbers.

Within this formulation, the sufficient condition for the Chambolle-Pock algorithm to converge is $\nu\mu < 1$. Setting $\nu = 1$ and $\mu = 1/2$ fulfills this condition. Note that θ is set at 1, like in the third section of [40], and that it is possible to compute the proximal of the convex conjugate F^* of F with the relation $\text{prox}_{F^*}(\mathbf{f}) = \mathbf{f} - \text{prox}_F(\mathbf{f})$ for $\mathbf{f} \in \mathbb{R}^N$.

1) *Choice of regularization criterion*: The new regularization scheme presented in this paper has various advantages: the CI constraint prevents from over-smoothing and the reconstruction scheme is generic in terms of the regularization function to use (with the only limit being to find an algorithm to solve Eq. (9) with the chosen ϵ_2).

As opposed to the widely used Tikhonov-like regularization functions, TV functions better preserve sharp edges and object boundaries that are usually the most important features to recover. Indeed, as the radiotracer activity distribution could be well-grounded considered as a piece-wise constant function, reconstructing sparse gradient-magnitude images seems to be completely relevant. In this paper, the usual discrete TV presented first in [41] was chosen as regularization function ϵ_2 , which is defined as the \mathcal{L}_1 norm of the discrete gradient of image \mathbf{f} . Note that quadratic or more complex convex penalties would also perfectly fit within the proposed approach.

Considering this choice, Eq. (9) becomes:

$$\min_{\mathbf{f} \in \mathbb{R}^N} TV(\mathbf{f}) + g_{[\mathbf{f}]}(\mathbf{f}), \quad (11)$$

2) *Choice of the interval inclusion constraint*: In Eq. (11), it is mandatory to formulate the data-fitting constraint in terms of the attachment function. In this paper, we propose two different choices for function g . As the density probability of the true distribution within the intervals is unknown, according to the Laplace principle, it is more judicious to consider the values within the CI as equally likely. The most intuitive approach is to constrain the TV regularized solution to be strictly included within the intervals $[\mathbf{f}]$. In the following, this constraint will be denoted "Hard Constraint" (HC). The second data-fitting constraint proposes to take into account the fact that the reconstructed intervals $[\mathbf{f}]$ are not 100% intervals and to authorize the solution to go beyond the CI. We propose to quadratically penalize the solution in this case. In the following, this constraint will be denoted "Soft Constraint" (SC).

The HC constraint can be expressed using the convex indicator function $i_{[\mathbf{f}]}$ defined as :

$$g_{[\mathbf{f}]}^{\text{HC}}(\mathbf{f}) = i_{[\mathbf{f}]} : \mathbf{f} \mapsto i_{[\mathbf{f}]}(\mathbf{f}) = \begin{cases} 0 & \text{if } \mathbf{f} \in [\mathbf{f}], \\ +\infty & \text{if } \mathbf{f} \notin [\mathbf{f}]. \end{cases} \quad (12)$$

$g_{[\mathbf{f}]}^{\text{HC}}$ imposes the regularized solution (i.e. the function that minimizes the TV in Eq. (11)) to strictly remain within the reconstructed interval-valued image $[\mathbf{f}]$.

To take into account the fact that the reconstructed intervals $[\mathbf{f}]$ are not 100% intervals, the proposed SC constraint allows

the solution to go beyond the intervals. However, to ensure sufficient data-fitting, the SC constraint $g_{[\mathbf{f}]}^{\text{SC}}$ was defined as the squared Euclidean distance to the convex set $[\mathbf{f}]$:

$$g_{[\mathbf{f}]}^{\text{SC}}(\mathbf{f}) = \frac{1}{2}(d_{[\mathbf{f}]}(\mathbf{f}))^2, \quad (13)$$

with the Euclidean distance $d_{[\mathbf{f}]}(\mathbf{f})$ of \mathbf{f} to the convex set $[\mathbf{f}]$ being defined as $d_{[\mathbf{f}]}(\mathbf{f}) = \inf_{y \in [\mathbf{f}]} \|\mathbf{f} - y\|_2$. Considering the data-fitting constraint defined in Eq. (13) for solving Eq. (11), the regularized solution \mathbf{f} is free to vary inside the intervals. It is however quadratically penalized when going beyond the convex set $[\mathbf{f}]$ (the more the solution is far from $[\mathbf{f}]$, the more it is penalized).

The constrained TV reconstruction framework of Eq. (11) requires computation of the proximal operators of the discrete TV, HC and SC functions. prox_{TV} is easily computed using Chambolle-Pock like algorithms [40]. The TV reconstruction framework of Eq. (11) also requires the computation of $\text{prox}_{g_{[\mathbf{f}]}^{\text{HC}}}$ for HC or $\text{prox}_{g_{[\mathbf{f}]}^{\text{SC}}}$ for SC.

From Chapter 10 of [42], the proximity operator $\text{prox}_{g_{[\mathbf{f}]}^{\text{HC}}}$ of the convex indicator function $g_{[\mathbf{f}]}^{\text{HC}}$ onto the closed and convex set $[\mathbf{f}]$ is the projection operator $P_{[\mathbf{f}]}(\mathbf{f})$ onto $[\mathbf{f}]$ with $[\mathbf{f}]$ being a nonempty subset of \mathbb{R}^N . $P_{[\mathbf{f}]}(\mathbf{f})$ is defined as the only point verifying $d_{[\mathbf{f}]}(\mathbf{f}) = \|\mathbf{f} - P_{[\mathbf{f}]}(\mathbf{f})\|_2$. The proximity operator of the squared distance to a convex set is also defined in [42].

Thus, the expression of both $\text{prox}_{g_{[\mathbf{f}]}^{\text{HC}}}$ and $\text{prox}_{g_{[\mathbf{f}]}^{\text{SC}}}$ proximal operators are:

$$\begin{aligned} \text{prox}_{g_{[\mathbf{f}]}^{\text{HC}}} &= P_{[\mathbf{f}]}(\mathbf{f}), \\ \text{prox}_{g_{[\mathbf{f}]}^{\text{SC}}} &= \frac{1}{2}(\mathbf{f} + P_{[\mathbf{f}]}(\mathbf{f})). \end{aligned} \quad (14)$$

Note that the 3D formulation of the proposed TV constrained reconstruction framework is rather straightforward for both CI reconstruction and TV constrained regularized selection.

C. Proposed reconstruction framework

This section presents how to practically reconstruct an image within the Regularized-Selection (RS) framework. The output of Algorithm 1 is the image \mathbf{f} obtained after regularizing the NIBEM (rsp. NIBART) algorithm with the RS procedure for both HC and SC constraints.

Algorithm 1 is composed of two successive iterative steps, each one is controlled by an iteration number. The first step is the CI reconstruction step. As the process is not regularized, an iteration number $ItRec$ needs to be set to stop the iterative process. In practice, $ItRec$ is chosen according to the value specified by the manufacturer for each corresponding usual algorithm (ie. ML-EM or SIRT). The second step is the TV constrained regularization step. For this step, there are two cases. When HC constraint is considered, the Chambolle-Pock minimization algorithm is run until convergence. In this case, the step is considered as regularization hyper-parameter free in the sense that no parameter is needed to set the balance between data-fitting and regularization level. In the second case, when considering the SC constraint, an iteration number

Algorithm 1 CI constrained TV regularization

Acquisition data: $[p] = [p, p]$
Input: Reconstruction iteration number: $ItRec$
Regularization iteration number: $ItReg$
Output: Regularized reconstructed image \mathbf{f}

FIRST STEP: CI constraint reconstruction

Initialization: $[\mathbf{f}^0] = [1_N, 1_N]$, 1_N being the ones matrix in \mathbb{R}^N

for $k = 0$ to $ItRec$ **do**

if (MLEM) **then**

$$[\mathbf{f}^{k+1}] = \mathcal{B}^*([p] \odot \overline{\mathcal{P}}([\mathbf{f}^k])) \boxtimes [\mathbf{f}^k]$$

else if (SIRT) **then**

$$[\mathbf{f}^{k+1}] = [\mathbf{f}^k] \boxplus \lambda \mathcal{B}^*([p] \odot \overline{\mathcal{P}}([\mathbf{f}^k]))$$

end if

end for

$$[\mathbf{f}] = [\underline{\mathbf{f}}, \bar{\mathbf{f}}] = [\mathbf{f}^{ItRec}]$$

SECOND STEP: TV constrained RS

Initialization: $v^0 = 0_N, n^0 = \mathbf{f}_{\text{center}}, w^0 = \mathbf{f}_{\text{center}}$, with 0_N being the zero matrix in \mathbb{R}^N and $\mathbf{f}_{\text{center}} = \frac{1}{2}(\underline{\mathbf{f}} + \bar{\mathbf{f}})$

for $i = 0$ to $ItReg$ **do**

$$v^{i+1} = v^i + w^i - \text{prox}_{\text{TV}}(v^i + w^i)$$

if (HC) **then**

$$n^{i+1} = \max(\min(n^i - \frac{1}{2}v^{i+1}, \bar{\mathbf{f}}), \underline{\mathbf{f}})$$

else if (SC) **then**

$$n^{i+1} = \frac{1}{2}(n^i - \frac{1}{2}v^{i+1} + \max(\min(n^i - \frac{1}{2}v^{i+1}, \bar{\mathbf{f}}), \underline{\mathbf{f}}))$$

end if

$$w^{i+1} = 2.n^{i+1} - n^i$$

end for

$$\mathbf{f} = n^{ItReg}$$

return \mathbf{f}

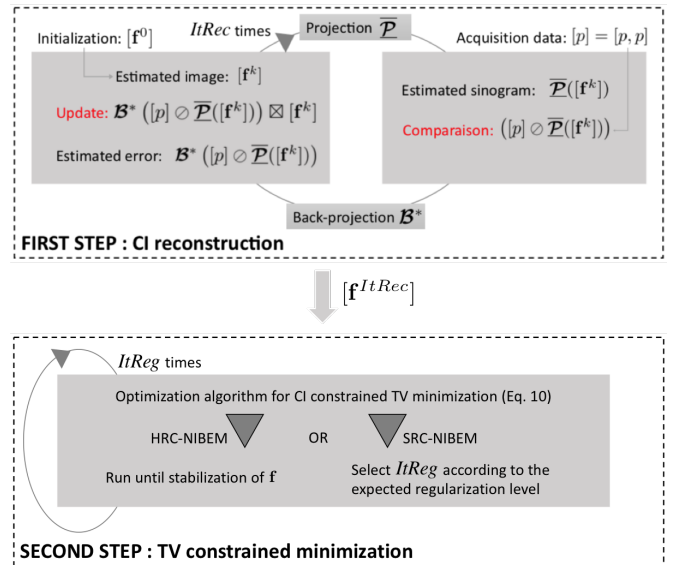


Fig. 1: Graphical illustration of HRS-NIBEM and SRS-NIBEM reconstruction algorithms

$ItReg$ has to be set to control the regularization level of solution f . The more iterations are performed, the more f is regularized. As this step is computationally inexpensive, one could imagine letting the physician decide which iteration corresponds to the desired regularization level.

In the following, NIBEM reconstruction using an HC constraint for RS will be denoted HRS-NIBEM. When instead using the SC constraint, the algorithm will be denoted SRS-NIBEM. For the experiments, the $prox_{TV}$ implementation proposed in [43], [44] was used.

III. EXPERIMENTS

Experiments were carried out to validate the proposed regularization scheme and to quantitatively compare the proposed method with usual ML-EM early-stop, Gaussian post-smoothing and MAP-EM-OSL reconstruction using quadratic [11] and TV [45] priors. Quantitative results were also compared to a recent patch-based reconstruction method [14]. The first experiment, presented in Section III-A aimed to investigate the behavior of the proposed regularized reconstruction scheme in terms of the spatial bias/variance trade-off. In the second experiment, in Section III-B, the sensitivity to partial volume effect of the proposed methods is addressed.

A. Spatial bias/variance trade-off

For this experiment, we investigated the behavior of the proposed CI based constrained TV regularization in terms of spatial bias and variance. In the first experiment of this section, we compared the Contrast Recovery Coefficient (CRC) as a function of the regularization weighting parameters of the proposed reconstruction scheme to other regularization methods. As the spatial bias/variance trade-off is difficult to evaluate, we propose to use the spatial bias and variance estimation of HRS-NIBEM reconstructions as a reference since this method does not require parameters to set the regularization level (the only parameter ($ItRec$) to select is chosen in accordance with the value specified by the manufacturer for ML-EM). First, we found the parameter for usual regularization methods to reach the same variance level as the reference one and compared the corresponding bias. Then we compared, for all tested methods, the best bias level obtained and the corresponding variance level.

1) *Experimental setup*: For this experiment, two different phantoms were simulated: an analytical Jaszczak phantom simulation and a more realistic Hoffman phantom acquisition using [35]. A physical Jaszczak phantom acquisition was also performed in clinical routine conditions to validate the experiments using real data.

The Jaszczak-like phantom consisted of a 2D uniform disk of 160 mm diameter including six hot regions with diameters of 9.5, 11.1, 12.7, 15.9, 19.1 and 25.4 mm. The hot region concentration was 4 times greater than the background concentration (Fig.2a). The Jaszczak-like phantom was digitalized into a 128x128 image with 1.563 mm pixel size. The sinogram was simulated with 128 linearly sampled detector bins and 128 angular views evenly spaced over 180° . The projection matrix was computed using a rectangular measurement model,

implemented as described in [46]. Photon attenuation and scatter were not simulated. Two different count levels were simulated using a Poisson random generator (100k and 1M expected events in the projection data).

2D PET data for the Hoffman phantom were simulated using a realistic GATE [35] model of the Siemens Biograph PET scanner. Only one slice of the phantom (Fig.2b) was considered for this experiment and only coincidences located within that cross-section were recorded. Two different count levels were simulated (1M and 3M counts). Acquisitions were corrected for attenuation, normalization, scatter and random.

The real Jaszczak phantom acquisition was performed using a Siemens Biograph mCT20Flow. ^{18}F FDG was injected in the phantom in order to obtain a 4:1 concentration ratio between the hot spheres and the background. In this experiment, only the four biggest spheres of the Jaszczak were used. Acquisitions were corrected for attenuation, normalization, scatter and random. 2D reconstructions were performed after FORE rebinning [47] of the 3D data. In the following experiments, we considered the transaxial slice that includes the centers of the hot spheres.

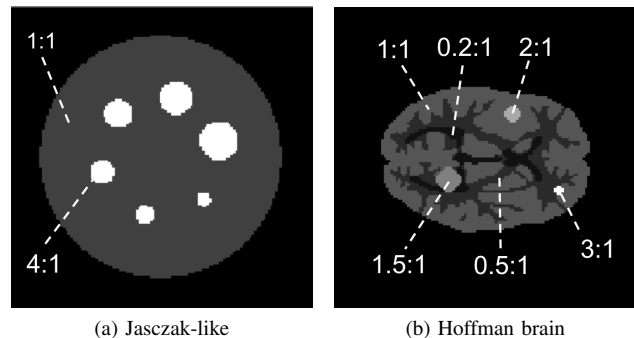


Fig. 2: Simulated phantoms and activity ratios

2) *Data analysis*: In order to quantitatively compare the performance of the proposed method with other usual regularization methods, we propose here to compare the mean tumor Contrast Recovery Coefficient (CRC) versus the Standard Deviation (SD) of a background region with uniform expected activity values. For the Jaszczak phantom, we compared the mean (CRC) in the hot spheres (4:1 ratio) versus a square patch of background (1:1 ratio) located at the center of the image. For the Hoffman phantom, we investigated the mean CRC in the bigger tumor (1.5:1 ratio) versus the gray matter (1:1 ratio) region considered as background. For real data, we used the same methodology as for Jaszczak phantom. Inspired by [14], the CRC, for the regularized reconstructed image was computed as:

$$CRC = \frac{|A_{tumor} - A_{background}|_1}{CR_0 \times A_{background}}, \quad (15)$$

with CR_0 being the normalization ratio between the expected tumor and the background activity (3 for simulated Jaszczak phantom and real acquisition, 0.5 for the Hoffman experiment), A_{tumor} the mean activity value in the Region Of

Interest (ROI) $tumor$, and $A_{background}$ the mean activity value in the background.

Plots in Fig. 3 show the CRC versus the SD of the background when varying the regularization weighting parameter of the corresponding method. For early-stop, the number of iterations of the ML-EM reconstruction was used as a regularization weighting parameter. For Gaussian post-smoothing, the regularization weighting was performed by varying the SD σ of the filtering Gaussian kernel. For MAP-EM-OSL and patch-based edge-preserving reconstructions, the regularization weighting parameter is denoted β . For the proposed methods, HRS-NIBEM is considered regularization hyper-parameter free as RS is run until convergence. For SRS-NIBEM, the regularization level is set by the the number of RS iterations.

To obtain these curves, we computed one noisy simulation and two noise levels for each simulated phantom (100k and 1M in Fig. 3c and Fig. 3d for the Jaszczak phantom and 1M and 3M in Fig. 3a and Fig. 3b for the Hoffman phantom). Fig. 3e presents a comparison for real data acquisitions.

The behavior of the proposed method with respect to the bias/variance tradeoff is highlighted by comparing the values of normalized mean absolute error (NMAE) and normalized mean variance (NMV) for the different regularization methods. NMAE and NMV are respectively defined, for ROI R of N pixels, by:

$$\begin{aligned} NMAE_R &= \frac{1}{N} \sum_{i=1}^N \frac{|f_i - f^{true}|}{f^{true}}, \\ NMV_R &= \frac{1}{N} \sum_{i=1}^N \frac{(f_i - f^{mean})^2}{f^{true}}, \end{aligned} \quad (16)$$

with f^{true} being the ground truth value in uniform ROI R, f^{mean} being the mean reconstructed value in uniform ROI R and f_i the reconstructed value of the i^{th} pixel in uniform ROI R.

Considering two different ROIs representing tumors and gray matter in realistic GATE simulations of 3M counts of the Hoffman phantom (Fig. 2b), we tried to recover the regularization parameters of the usual methods and SRS-NIBEM that allow reconstruction of the images with the same NMV as the HRS-NIBEM reference one. Results are presented in Table I.

3) *Results*: For each phantom and each noise level, Fig. 3 presents quantitative comparisons of the mean tumor CRC versus the SD of background noise as a function of the regularization weighting parameter for each tested reconstruction algorithm. The performance of RS-NIBEM regularization techniques are appealing. Indeed, for each of the simulations (Fig. 3a,3b,3c,3d) and real acquisitions (Fig. 3e), the CRC at any given background SD level is higher than the one obtained with usual regularization methods. For the HRS-NIBEM reconstructions, which do not make use of an hyper-parameter to set the balance between data-fitting and the regularization level, the CRC is higher than the other usual regularization schemes for the same background SD (except for Hoffman

1M, where HRS-NIBEM CRC is slightly lower than MAP-EM TV and the patch-based edge-preserving method [14]), thus highlighting the competitiveness of this method. The SRS-NIBEM reconstruction is likely to be more robust than usual regularization schemes, and the quality competitiveness of this approach in terms of CRC is even more noticeable for low SD values, thus highlighting that SRS-NIBEM allows us to reconstruct regularized images with a CRC in acceptable ranges. It is also interesting to note the CRC peak obtained for SRS-NIBEM in Fig.3b and Fig.3e, that can be considered as the rupture point of the balance between the data-fitting and regularization level. Indeed, from that point, SC allows TV regularization to get the upper hand on the data fitting constraint. Speaking of complexity, the computation time to obtain a reconstruction of Hoffman 3M phantom for MAP-EM TV algorithm lasted 7.5s. By comparison, 200 iterations of SRS-NIBEM lasted 46.1s (24.1s for NIBEM CI reconstruction and 22s for the 200 iterations of SRS).

To visually highlight the CRC comparison presented here, in Fig. 6 we present the reconstructions of ML-EM, HRS-NIBEM and SRS-NIBEM having the higher CRC for a real Jaszczak-like phantom. For better CRC levels, RS-NIBEM methods clearly achieve more interesting statistical variance levels.

Table I presents the NMAE obtained for each methods for the same NMV. For both tumors and gray matter, best results were obtained with SRS-NIBEM. The second better results were obtained with HRS-NIBEM for tumors but not for gray matter.

Globally, RS-NIBEM methods allow us to obtain better results than usual regularized reconstruction methods, for both uniform large regions (SRS-NIBEM should be preferred) and small tumors. As expected, HRS-NIBEM gives interesting results for small tumors because the HC constraint prevents the solution from over-smoothing and thus tends to prevent the reconstructions from partial volume effects. However, SRS performs better, for the same NMV level, than HRS-NIBEM in terms of NMAE, especially in large uniform regions. Indeed, as the gray matter is a large and uniform ROI, the TV regularization term associated with the SC constraint allows to better recover the uniformity of the ROI because the penalty substantially reduces the perturbation of noisy pixels for which the ground truth is not included in the intervals reconstructed with NIBEM.

To visually highlight the results showed here, in Fig. 4, we present the reconstructions with same variance level ($NMV \approx 1.5$) as HRS-NIBEM in gray matter (1:1 ratio) of 3M counts of the Hoffman phantom.

In the last experiments, we investigated the NMAE obtained for the same NMV with different reconstruction algorithms. Now, for each algorithm, we computed reconstructions until reaching the regularization hyper-parameter that allows us to obtain the smallest global NMAE possible. Considering the corresponding reconstructions of 100k Jaszczak phantom, we compared the best achievable global NMAE and the NMV in the background (1:1 ratio) between the different reconstruction algorithms. The best results were obtained with RS-based methods and MAP-EM TV. The corresponding reconstructions

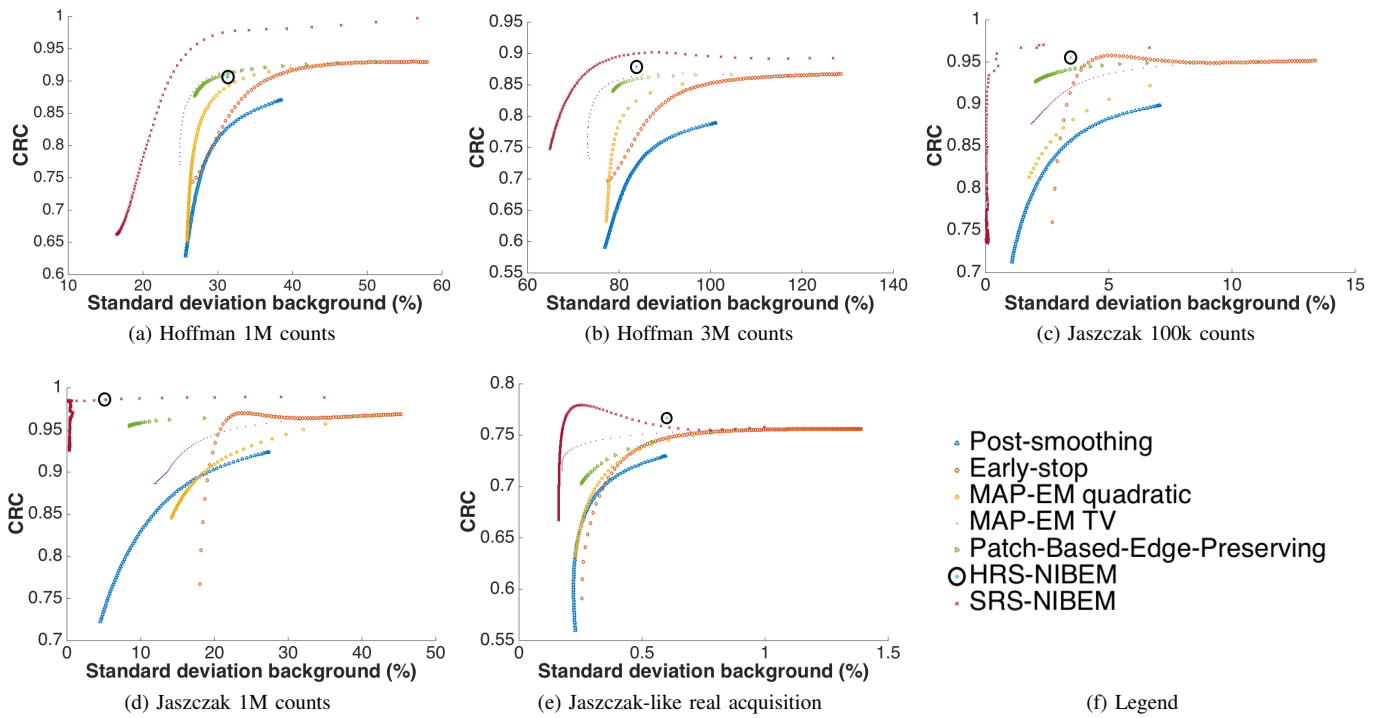


Fig. 3: Contrast recovery curves of tumor (Hoffman phantom) and hot spheres (Jaszczak phantoms) versus background SD for the different regularization techniques. The curves were obtained by varying the corresponding regularization weighting parameters.

ROI		HRS-NIBEM	MAP-EM quadratic	MAP-EM TV	Patch-based [14]	Early-stop	SRS-NIBEM
Tumor 3:1 ratio	Regularization parameter	free	$\beta = 0.003$	$\beta = 0.1$	$\beta = 0.07$	It = 53	ItReg = 21
	NMV	1.656	1.567	1.658	1.604	1.650	1.614
	NMAE	0.361	0.432	0.388	0.390	0.434	0.344
Tumor 2:1 ratio	Regularization parameter	free	$\beta = 0.013$	$\beta = 0.4$	$\beta = 0.6$	It = 22	ItReg = 20
	NMV	0.891	0.873	0.901	0.898	0.870	0.894
	NMAE	0.177	0.193	0.187	0.186	0.197	0.162
Gray matter 1:1 ratio	Regularization parameter	free	$\beta = 0.025$	$\beta = 0.4$	$\beta = 0.6$	It = 21	ItReg = 15
	NMV	1.501	1.500	1.490	1.490	1.501	1.509
	NMAE	0.165	0.162	0.158	0.160	0.155	0.155

TABLE I: Quantitative bias-variance tradeoff comparison for different ROI of 3M counts Hoffman phantom simulation.

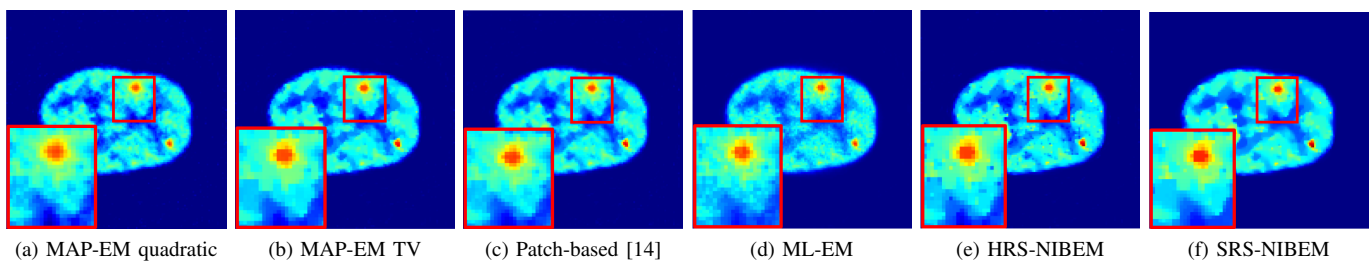


Fig. 4: Typical reconstructions with regularization parameters chosen to obtain the same spatial variance (NMV=1.5) in the gray matter of an Hoffman brain acquisition for 3M counts. The same colorscale was used for all figures.

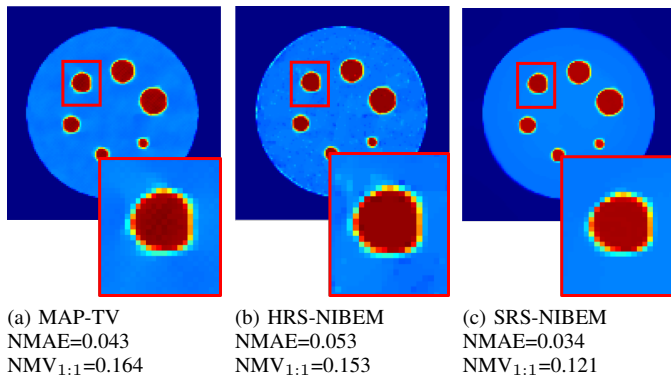


Fig. 5: Typical reconstructions with regularization parameters chosen to obtain lower global NMAE possible for 100k Jaszczak simulation (only MAP-TV, HRS-NIBEM and SRS-NIBEM are presented since they provided the best results in terms of global NMAE here). NMV values in the background (1:1 ratio) for the same parameters are also displayed. The same colorscale was used for all figures.

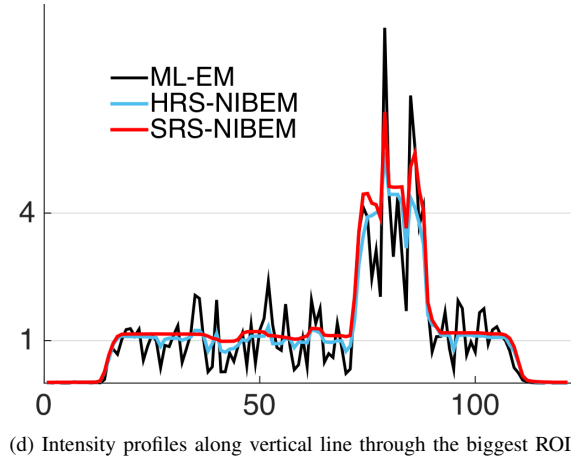
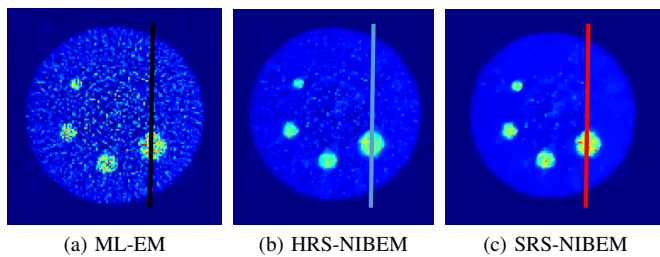


Fig. 6: Real Jaszczak-like reconstructions with higher CRC for a) ML-EM, b) HRS-NIBEM and c) SRS-NIBEM and d) horizontal profiles through the center of the biggest hot sphere. For visualization matter, data were normalized in order to obtain a mean background value of 1. Ratio expected between hot sphere and background is 4:1.

are presented in Fig. 5. Other usual methods gave the following results: MAP-EM quadratic: NMAE=0.089, NMV_{1:1}=0.350; Gaussian smoothing: NMAE=0.093, NMV_{1:1}=0.479; ML-EM: NMAE=0.086, NMV_{1:1} = 0.256. Thus, except for MAP-

EM TV which also gives interesting results, SRS-NIBEM performs two times better in terms of global NMAE and NMV in the background than the usual regularization methods. For HRS-NIBEM, the quantitative improvement is about 60% in terms of global NMAE and background NVM. As mentioned, for this experiment where “ \mathcal{L}_1 like” priors are more adapted, MAP-EM TV gives interesting results, but still not as effective as those of SRS-NIBEM. Interesting quantitative properties have been found for both HRS-NIBEM and SRS-NIBEM reconstructions, however it is worth mentioning that point-like artifacts can be present in HRS-NIBEM reconstructions (Fig.4e,5b). SRS-NIBEM was designed to reduce these artifacts. It gave both quantitatively (Table. I) and qualitatively (Fig.4e,5c,9c,9f) improved results when choosing the optimal *ItReg* parameter. As the computational cost to perform SRS-NIBEM reconstructions for different regularization levels is relatively low, SRS-NIBEM seems a better option for clinical use. Indeed, the choice of regularization level could be left to the physician as it is directly related to the iteration number of the second step. This operation would be computationally inexpensive as it only consists of saving all iterations of the SRS step.

B. Statistical sensitivity to partial volume effects

After investigating the spatial bias and variance properties of the propose RS-NIBEM framework, we proposed in this section to investigate the sensitivity to partial volume effects of the reconstructed estimates.

1) *Simulated setup*: For this experiment, we used the same simulation setup as in Section III-A1. In order to investigate the statistical variability of the estimates, we simulated, for both Jaszczak and Hoffman phantoms, $K = 100$ statistical replicates for each considered count level.

2) *Data analysis*: For the Jaszczak phantom, for the K reconstructions performed, for each sphere section $i \in \{2,4\}$ (with i being the index of the sphere sections from smallest to biggest), the Central Intensity Recovery $CIR_{p_i,k}$ for the central pixel p_i of each sphere of index i , for each replicate k , was computed as:

$$CIR_{p_i,k} = \frac{f_{p_i,k}}{f_{p_i}^{true}}, \quad (17)$$

with $f_{p_i,k}$ being the intensity value of pixel p_i for replicate k , and $f_{p_i}^{true}$ being the ground truth expected value for this same pixel.

For the Hoffman phantom, we also computed $CIR_{p_i,k}$ as in Eq. 17, for each tumor $i \in \{2,3\}$ (with i being the index of the tumor from the smallest activity ratio (1.5:1) to the highest activity ratio (3:1) as displayed in Fig. 3).

The parameters that allow us to achieve the smallest global NMAE in the whole image of the first replicate for both Jaszczak and Hoffman phantoms were used for this experiment.

To quantitatively compare the sensitivity of the reconstruction methods in terms of partial volume effect, we computed the SRC through the K repetitions for each ROI of each phantom. The results are presented in Fig. 7 for Jaszczak phantoms and in Fig. 8 for Hoffman phantoms.

3) *Results:* Concerning Jaszczak phantoms, the statistical sensitivity of the reconstructed estimates to partial volume effects using the proposed approach is appealing. Indeed, HRS-NIBEM and SRS-NIBEM CIRs are always better than CIRs obtained with usual methods either for mean bias or dispersion. While the mean bias obtained with HRS-NIBEM and SRS-NIBEM are slightly higher than those obtained with the usual method, the difference remains in a reasonable range. This statement is valid for both count levels. Dispersion is always smaller for SRS-NIBEM, and comparable to that obtained with the most efficient usual regularization scheme in terms of CIR for HRS-NIBEM.

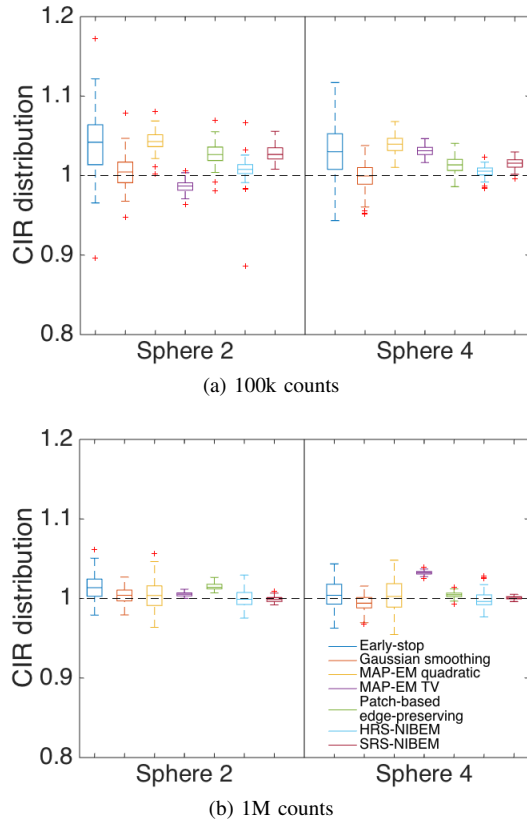


Fig. 7: CIR for Jaszczak phantoms

Experiments carried out on the more realistic Hoffman phantom confirmed this trend. Quantitative results of statistical sensitivity to partial volume effects for both SRS-NIBEM and HRS-NIBEM reconstruction techniques are appealing in terms of mean bias, with a reasonable estimated dispersion. In terms of dispersion, they are overtaken by MAP-EM methods and patch-based edge-preserving method that however give worse CIR mean bias.

For visual assessment of the proposed framework, real data acquired with a Siemens Biograph mCT 20 Flow scanner 30 minutes after injection of 2.5 Mbq/Kg of ^{18}F -FDG were reconstructed using the proposed framework. Typical reconstructions of a transaxial-slice of a healthy control and a patient suffering from Alzheimer disease in clinical acquisition conditions are presented in Fig. 9. Reconstructions are qualitatively compatible with clinical routines.

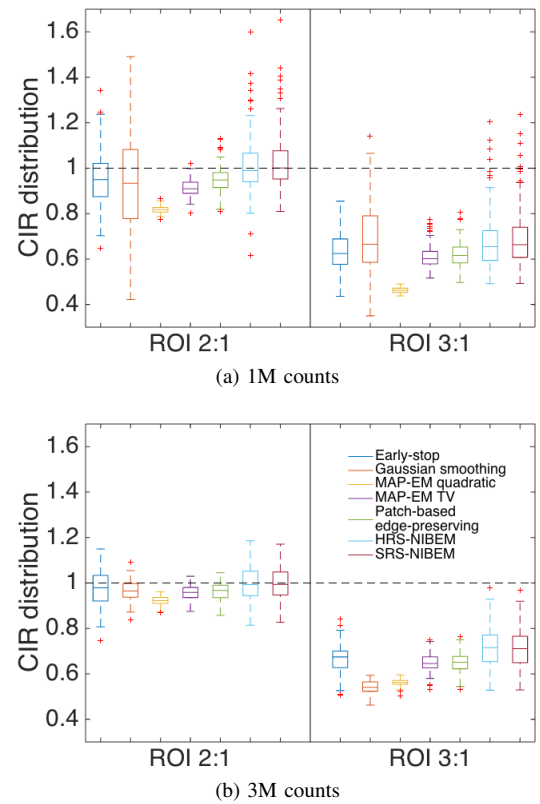


Fig. 8: CIR for Hoffman phantoms

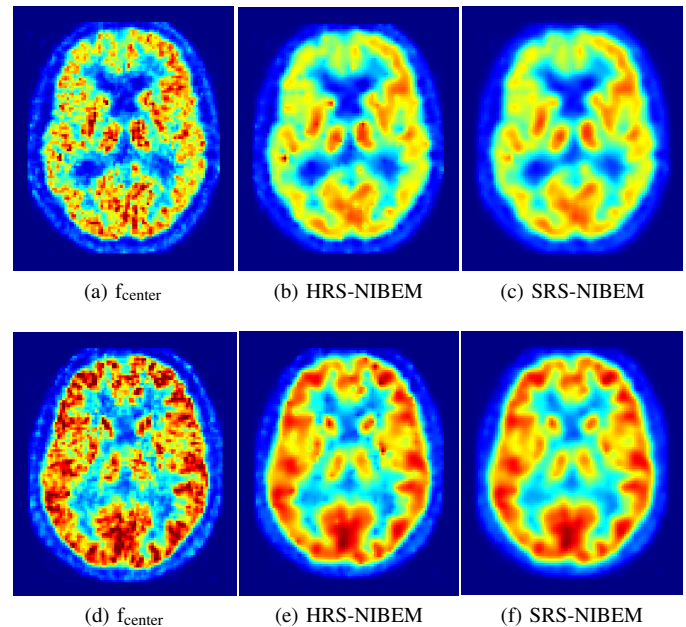


Fig. 9: Reconstruction of a trans-axial slice of a healthy control (bottom row) and an Alzheimer's disease patient (top row). Data were acquired in clinical setting and reconstructed using the proposed framework. (a) and (d) are obtained in output of the first step. (b,c,e,f) are reconstructed with image smoothness compatible with visual interpretation. The same colormap is used for all of the presented slices.

IV. CONCLUSION

We proposed in this paper a new framework for PET reconstruction involving CI-based constrained TV regularization. One of the features of the proposed methodology lies in the fact that the reconstruction scheme is a two-step process. We propose first to focus on reconstructing a convex-set of admissible solutions that ensure the data fidelity and then, in a second step, to select the most appropriate image according to a regularization criterion under the constraint established in step one.

In this paper, the proposed methodology was put into practice using, for the first step, a new class of algorithms that focus on statistical noise quantization. It makes it possible to reconstruct stable and reliable CI. For the second step, the widely used TV regularization function was used. In particular, we investigated the properties of RS-NIBEM algorithms in terms of the spatial and statistical bias/variance trade-off. We showed with simulated and real data that HRC-NIBEM reconstructions have appealing properties compared to the usual regularization schemes in terms of the bias/variance balance. The combination between the hard constraint and the reconstructed CI used in this framework allows for the design of a regularized algorithm that does not make data-fitting compromises when regularizing the solution. Indeed, the CI-constraint is a guarantee that over-smoothing will not occur. An alternative to the hard constraint was also proposed. The proposed soft constraint takes into account the fact that currently reconstructed CI are not 100% CI. The SRS-NIBEM allows us to reconstruct images with even more accurate variance levels, keeping bias in reasonable ranges compared to usual regularization procedures. Within this configuration, the regularization level needs to be set by early-stopping the second step. However, the optimization algorithm used [40] was proven to be fast and efficient. It is thus straightforward to reconstruct and select the reconstruction that best fits the expected level of regularization.

RS-NIBEM has a potential scope of applications in detecting small lesions, which is particularly relevant for oncological imaging in which partial volume effects appear critical. Low-dose PET reconstruction would undoubtedly benefit from such an approach.

To conclude, it is also important to mention that the proposed framework is generic. Indeed, it would benefit from further work on CI reconstruction and from using more sophisticated regularization functions such as [48]. The HRS-NIBEM algorithm would still benefit from its over-smoothing prevention nature. Nevertheless, other more complex soft constraints could be worth considering by for example, making use of prior anatomical information knowledge obtained by using anatomical imaging such as CT or MR. Within this framework, design of regularization procedures for specific clinical application tasks could also be the focus of further studies.

ACKNOWLEDGMENT

This work was partially supported by the Siemens Healthineers company. The authors would like to gratefully thank Marjolaine Fourcade for her help on real data acquisition.

REFERENCES

- [1] L. Strauss and P. Conti, "The application of PET in clinical oncology," *Journal of Nuclear Medicine*, vol. 32, pp. 623–648, 1991.
- [2] R. Gordon, R. Bender, and G. Herman, "Algebraic reconstruction techniques (art) for three dimensional electron microscopy and x-ray photography," *Journal Theor. Bio.*, vol. 36, p. 105–117, 1970.
- [3] A. Lakshminarayanan and A. Lent, "Methods of least squares and sirt in reconstruction," *Journal Theor. Bio.*, vol. 76, no. 3, pp. 267–295, 1979.
- [4] L. Shepp and Y. Vardi, "Maximum likelihood reconstruction for emission tomography," *IEEE Trans. Medical Imaging*, vol. 1, no. 2, pp. 113–122, 1982.
- [5] K. Lange and R. Carson, "Em reconstruction algorithms for emission and transmission tomography," *Journal of Computer Assisted Tomography*, vol. 2, no. 8, 1984.
- [6] A. Nemirovskii, "The regularization properties of adjoint gradient method in ill-posed problems," *USSR Computational Mathematics and Mathematical Physics*, vol. 26, no. 2, pp. 7–16, 1986.
- [7] H. Flemming, "Equivalence of regularization and truncated iteration in the solution of ill-posed image reconstruction problems," *Linear Algebra Appl.*, vol. 130, pp. 133–150, 1990.
- [8] A. de Decker, J. A. Lee, and M. Verlysen, "Variance stabilizing transforms in patch-based bilateral filters for Poisson noise image denoising," in *Engineering in Medicine and Biology Society Conf.* IEEE, 2009.
- [9] J. Kim, I. Ahn, W. Nam, Y. Chang, and J. Ra, "Post-filtering of PET image based on noise characteristic and spatial sensitivity distribution," in *Nuclear Science Symposium and Medical Imaging Conference (NSS/MIC)*. IEEE, 2013.
- [10] T. Hebert and R. Leahy, "A generalized EM algorithm for 3D bayesian reconstruction from poisson data using Gibbs priors," *IEEE Trans. Medical Imaging*, vol. 8, pp. 194–202, 1989.
- [11] P. J. Green, "Bayesian Reconstructions From Emission Tomography Data Using a Modified EM Algorithm," *IEEE Trans. Medical Imaging*, vol. 9, pp. 84–93, 1990.
- [12] J. Qi and R. Leahy, "Resolution and noise properties of map reconstruction for fully 3-d PET," *IEEE Trans. Medical Imaging*, vol. 19, no. 5, pp. 493–506, 2000.
- [13] J. Fessler, "Penalized weighted least squares image reconstruction for positron emission tomography," *IEEE Trans. Med. Imaging*, vol. 13, pp. 290–300, 1994.
- [14] G. Wang and J. Qi, "Penalized Likelihood PET Image Reconstruction Using Patch-Based Edge-Preserving Regularization," *IEEE Trans. Med. Imaging*, vol. 31, no. 12, pp. 194–204, 2012.
- [15] M. Rani, S. B. Dhok, and R. B. Deshmukh, "A systematic review of compressive sensing: Concepts, implementations and applications," *IEEE Access*, vol. 6, pp. 4875–4894, 2018.
- [16] C. R. Vogel and M. E. Oman, "Iterative Methods for Total Variation Denoising," *SIAM J. Sci. Comput.*, vol. 17, no. 1, pp. 227–238, 1996.
- [17] D. Donoho, I. Johnstone, and I. M. Johnstone, "Ideal spatial adaptation by wavelet shrinkage," *Biometrika*, vol. 81, pp. 425–455, 1993.
- [18] D. Donoho, "Compressed sensing," *IEEE Transactions on Information Theory*, vol. 52, no. 4, pp. 1289–1306, 2006.
- [19] T. F. Chan, G. H. Golub, and P. Mulet, "A Nonlinear Primal-Dual Method for Total Variation-Based Image Restoration," *SIAM J. Sci. Comput.*, vol. 20, no. 6, pp. 1964–1977, 1999.
- [20] P. L. Combettes and J.-C. Pesquet, "Image Restoration Subject to a Total Variation Constraint," *IEEE Transactions on Image Processing*, vol. 13, no. 9, 2004.
- [21] H. A. Aly and E. Dubois, "Image up-sampling using total-variation regularization with a new observation model," *IEEE Transactions on Image Processing*, vol. 14, no. 10, pp. 1647–1659, 2005.
- [22] M. K. Ng, H. Shen, E. Y. Lam, and L. Zhang, "A Total Variation Regularization Based Super-Resolution Reconstruction Algorithm for Digital Video," *Journal on Advances in Signal Processing*, 2007.
- [23] A. Marquina and S. J. Osher, "Image Super-Resolution by TV-Regularization and Bregman Iteration," *Journal of Scientific Computing*, vol. 37, no. 367, 2008.
- [24] E. Sidky and X. Pan, "Image reconstruction in circular cone-beam computed tomography by constrained, total-variation minimization," *Phys. Med. Biol.*, vol. 53, pp. 4777–4807, 2008.
- [25] E. Sidky, J. Jørgensen, and X. Pan, "Convex optimization problem prototyping for image reconstruction in computed tomography with the Chambolle–Pock algorithm," *Phys. Med. Biol.*, vol. 57, no. 3065, 2012.
- [26] C. Wang, Z. Hu, P. Shi, and H. Liu, "Low dose pet reconstruction with total variation regularization," in *2014 36th Annual International Conference of the IEEE Engineering in Medicine and Biology Society, Aug 2014*, pp. 1917–1920.

- [27] M. Burger, J. Müller, E. Papoutsellis, and C.-B. Schönlieb, "Total Variation Regularisation in Measurement and Image space for PET reconstruction," *Inverse Problems*, vol. 30, no. 10, 2014.
- [28] G. Wang and J. Qi, "Edge-preserving PET image reconstruction using trust optimization transfer," *IEEE Trans. Medical Imaging*, vol. 4, no. 34, pp. 930–939, 2015.
- [29] F. Kucharczak, C. Mory, O. Strauss, F. Comby, and D. Mariano-Goulart, "Regularized selection: a new paradigm for inverse based regularized image reconstruction techniques," in *Image Processing (ICIP), 2017 IEEE International Conference on*. IEEE, 2017, pp. 1637–1641.
- [30] K. Bredies and M. Holler, "Artifact-free JPEG decompression with total generalized variation," *VISAPP*, pp. 12–21, 2012.
- [31] —, "A TGV-based framework for variational image decompression, zooming, and reconstruction. Part I: Analytics," *SIAM Journal on Imaging Sciences*, vol. 8, no. 4, pp. 2814–2850, 2015.
- [32] Z. Zhang, J. Ye, B. Chen, A. E. Perkins, S. Rose, E. Y. Sidky, C.-M. Kao, D. Xia, C.-H. Tung, and X. Pan, "Investigation of optimization-based reconstruction with an image-total-variation constraint in pet," *Physics in Medicine & Biology*, vol. 61, no. 16, p. 6055, 2016. [Online]. Available: <http://stacks.iop.org/0031-9155/61/i=16/a=6055>
- [33] O. Strauss, A. Lahrech, A. Rico, D. Mariano-Goulart, and B. Telle, "A new interval based algebraic reconstruction technique for error quantification of emission tomography images," *MICCAI*, 2009.
- [34] F. Kucharczak, K. Loquin, I. Buvat, O. Strauss, and D. Mariano-Goulart, "Interval-based reconstruction for uncertainty quantification in PET," *Physics in Medicine & Biology*, vol. 63, no. 3, 2018.
- [35] S. Jan, G. Santin, D. Strul, and al., "GATE: a simulation toolkit for PET and SPECT," *Phys. Med. Biol.*, vol. 49, pp. 4543 – 4561, 2004.
- [36] A. Rico, O. Strauss, and D. Mariano-Goulart, "Choquet integrals as projection operators for quantified tomographic reconstruction," *Fuzzy Sets and Systems*, vol. 160, no. 2, pp. 198–211, 2009.
- [37] K. Loquin, O. Strauss, and J. Crouzet, "Possibilistic signal processing: How to handle noise?" *International Journal of Approximate Reasoning*, vol. 51, no. 9, pp. 1129–1144, 2010.
- [38] D. Denneberg, *Non-additive measure and Integral*. Kluwer Academic Publishers, 1994.
- [39] P. L. Combettes, L. Condat, J.-C. Pesquet, and B. C. Vu, "A forward-backward view of some primal-dual optimization methods in image recovery." IEEE, Oct. 2014, pp. 4141–4145. [Online]. Available: <http://ieeexplore.ieee.org/document/7025841/>
- [40] A. Chambolle and T. Pock, "A first-order primal-dual algorithm for convex problems with applications to imaging," *Journal of Mathematical Imaging and Vision*, vol. 40, pp. 120–145, 2011.
- [41] L. Rudin, S. Osher, and E. Fatemi, "Nonlinear total variation based noise removal algorithms," *Physica D.*, vol. 60, pp. 259–268, 1992.
- [42] H. Bauschke, R. Burachik, P. Combettes, V. Elser, D. R. Luke, and H. Wolkowicz, *Fixed-Point Algorithms for Inverse Problems in Science and Engineering*. Springer-Verlag New York, 2011, vol. 49, no. 1.
- [43] A. Barbero and S. Sra, "Fast Newton-type Methods for Total Variation Regularization," in *ICML*, 2011.
- [44] —, "Modular proximal optimization for multidimensional total-variation regularization." [Online]. Available: <http://arxiv.org/abs/1411.0589>
- [45] V. Panin, Z. G.L., and G. G.T., "Total Variation Regulated EM Algorithm," *IEEE Trans. on Nuclear Science*, vol. 46, no. 6, pp. 2202–2210, 1999.
- [46] J. Fessler, "Aspire 3.0 user's guide: a sparse iterative reconstruction library," Department EECS, University of Michigan, Ann Arbor, Tech. Rep. 293, 1995.
- [47] D. T. M. DeFrise, P.E. Kinahan, C. Michel, M. Sibomana, and D. Newport, "Exact and approximate rebinning algorithms for 3-D PET data," *IEEE Trans. Med. Imaging*, vol. 16, no. 2, pp. 194–204, 1997.
- [48] K. Bredies, K. Kunisch, and T. Pock, "Total Generalized Variation," *SIAM J. Imaging Sci.*, vol. 3, no. 3, pp. 492—526, 2010.